energy&fuels

pubs.acs.org/EF Article

Investigation of Combined Capture−Destruction of Toluene over Pd/MIL-101 and TiO_2/MIL-101 Dual Function Materials

Busuyi O. Adebayo, Anirudh Krishnamurthy, Qasim Al-Naddaf, Ali A. Rownaghi, and Fateme Rezaei*

Cite This: https://doi.org/10.1021/acs.energyfuels.1c01950 Read Online

ACCESS | Metrics & More | Article Recommendations | Supporting Information

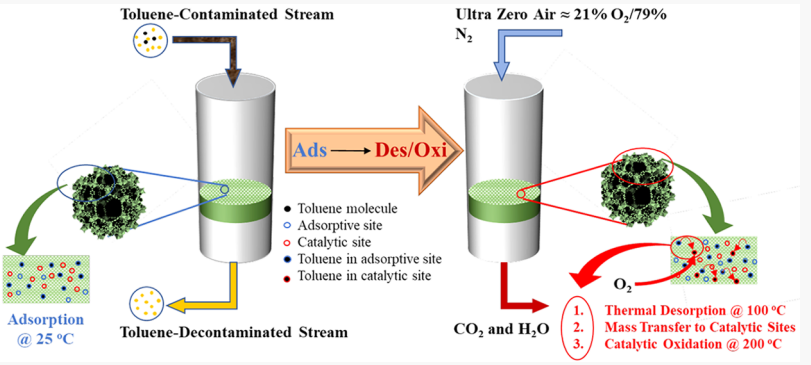

ABSTRACT: Combined capture−destruction strategies offer a sustainable approach to abate volatile organic compounds (VOCs) in a cost-effective manner. In this work, we investigated the potential of metal/MOF and metal oxide/MOF as dual function materials for use in a combined capture−destruction process to abate toluene emissions. Specifically, to enhance the catalytic activity of the MOF, 18 wt % TiO_2 and 0.7 wt % Pd were loaded onto the surface of MIL-101(Cr) and were investigated for their toluene capture and oxidation potential. As a means of achieving complete destruction, a desorption process was facilitated with simultaneous oxidation. The sequential adsorption-oxidation tests revealed that although the capture capacity decreases upon the addition of TiO_2 and Pd to the MOF, its catalytic activity increases substantially. At low concentrations of toluene, for example, the 500 ppm_v used in this study, bare MIL-101(Cr) exhibited the highest equilibrium uptake at 5.6 mmol/g at 25 °C, whereas Pd/MIL-101(Cr) and TiO_2/MIL-101(Cr) exhibited only 3.6 and 1.2 mmol/g uptake capacity, respectively, under the same conditions. On the contrary, Pd/MIL-101(Cr) outperformed the other materials by displaying a TOF value of 1.32 $mmol_{C7H8}/mol_{AS}/s$, which was 10% and 15% higher than those of TiO_2/MIL-101(Cr) and MIL-101(Cr), respectively. Overall, the obtained results highlight the efficacy of metal/metal oxide-MOF composites as dual function materials for the efficient capture and destruction of VOCs from ultradilute streams.

1. INTRODUCTION

Among various volatile organic compounds (VOCs) exhausted from common sources, benzene, toluene, and xylene (BTX) compounds are quantitatively one of the largest emissions.[1,2] Toluene in particular is used as a chemical feedstock to produce benzene. While airborne toluene is a notorious pollutant, the largest concentrations of toluene are found in the indoor environment due to its emission from common household items and was found to be around 31.5 $\mu g/m^3$.[3] Toluene abatement has been thoroughly studied in the past.[3] The commonly used methods, in terms of a process perspective, can be classified into separation and destruction processes. The former includes absorption,[4] adsorption,[5] biofiltration,[6] and membrane technology,[7] whereas the latter includes thermal oxidation and catalytic oxidation,[8] which is further divided into many subparts. Among these operations, physical adsorption has been identified to be a candidate for the separation of VOCs and other pollutants at dilute concentrations due to high adsorbate recoverability which results in a more cost-effective separation process.[9]

One of the most frequently used materials in toluene adsorption are carbonaceous materials such as activated carbon and graphene-based materials owing to their low cost, abundance, and efficient abatement performance.[10−13] Ordered mesoporous silica-based materials have also shown efficacy in abating toluene vapor.[14,15] Similarly, zeolites have also been investigated for their potential for toluene capture, albeit to a lesser extent than other materials.[16] Metal-organic

Received: June 15, 2021
Revised: July 15, 2021

frameworks (MOFs), on the other hand, have been extensively studied for the adsorption of many aromatic VOCs, toluene in particular.[17−20] MIL-101(Cr) and its variants with its superior surface qualities[20,21] have been investigated frequently for toluene capture.[22] For instance, in a study by Bahri et al.,[23] MIL-101(Cr) exhibited a maximum equilibrium uptake of 23 mmol/g when exposed to 1 ppm toluene gas, quantitatively larger than all other MOFs tested. The ability of MOFs to be functionalized is a defining character of these materials and is generally done to enhance their performance.[24] In this regard, Hu et al.[25] synthesized nanoscale titania mounted on MIL-101(Cr) for the degradation of formaldehyde. The impregnation of titania was shown to increase the degradation capacity of formaldehyde and o-xylene on bare MIL-101(Cr). In another investigation, Qin et al.[26] used a sol−gel method to immobilize $PdCl_2$ and Pd nanoparticles on the surface of MIL-101(Cr) to determine the toluene and hydrogen capture potentials. It was hypothesized that the π-complexation between the $PdCl_2$ and the aromatic toluene caused an increase in toluene uptake potential in $PdCl_2$/MIL-101(Cr).

Hybrid separation−reaction processes that take advantage of dual function materials (DFMs) with adsorptive and catalytic functionalities offer a sustainable, cost-effective approach to optimize the overall process efficiency. Such hybrid systems have been widely investigated in other applications including carbon capture utilization.[27−30] In our earlier investigations, we also demonstrated the applicability of this approach for capture and oxidation of aromatic VOCs including toluene and benzene over mixed-metal oxides.[31,32] For such hybrid processes to outcompete the conventional abatement or destruction technologies, the DFMs should possess balanced properties between capture and destruction (optimal adsorption and maximal destruction properties). Moreover, the materials should not only have high and selective capture capacities but should also have high catalytic activities without any release of the captured VOCs or regeneration of secondary pollutants. In other configurations such as a two-beds−one-column reactor, adsorption is performed in the adsorbent bed (the first/upstream bed), followed by reaction in the catalyst bed (the second/downstream bed).[33,34] VOCs' desorption from the first bed is then carried out by lowering the reactor into a furnace so that the two beds are heated at the reaction temperature. The desorbed VOC is then carried to the second bed for catalytic oxidation to take place. In the two-beds−two-columns configuration, adsorption is carried out in the first bed. Thereafter, the bed undergoes desorption, and its effluent is then passed through the second bed (already equilibrated at the reaction temperature) for catalysis to take place.[35] Although these reactor configurations have been proven to be successfully operated, clearly, they give no room for process integration between endothermic desorption and exothermic oxidation and thus can be cost intensive. The third configuration is the one-bed−one-column reactor.[36−38] In this configuration, adsorption and desorption/catalysis occur sequentially in the same bed. This has the advantages of process integration and thus can be energy and cost efficient. However, designing and operating such a configuration has posed a challenge especially when the adsorption and the reaction temperatures are widely different, due to the high tendency for thermal runaway of the desorbed VOCs before the catalyst attains its activity temperature (the light-off temperature). From a design perspective, the best way to overcome this drawback is to utilize a DFM with a catalyst activity temperature close to the intended adsorption temperature. Unfortunately, this is also very challenging. Till now, three different methods have been reported in the literature for designing a one-bed−one-column reactor. The simplest of these methods is the use of a single material that can act both as an adsorbent and as a catalyst. Although such materials are scarce, MIL-101[39] and hopcalite ($CuMn_2O_x$)[38] have been reported as such for toluene sequential adsorption and oxidation. Another common method is by a physical/mechanical admixture of adsorbent and catalyst.[28] However, the lack of optimal distribution of the admixture, leading to poor performance and hot-spot generation, has been reported by many authors to be the main setback of this method.[40] Other methods such as impregnation/doping of catalyst on the adsorbent, exchange of some sites on adsorbent with catalyst (e.g., metal-exchanged on zeolite), and cosynthesis of adsorbent and catalyst have been investigated as well.[31,32,41] From the process perspective, proper selection of operating conditions can limit the thermal runaway of the desorbed VOCs. For instance, the use of a low oxidant flow rate (e.g., 5%−30% of the adsorptive stream flow rate) has been suggested by Campbell and Sanders to circumvent the thermal runaway issue.[42]

In continuation of our investigation into sequential adsorption and oxidation of VOCs, we employed the one-bed−one-column reactor configuration and prepared three different materials, namely, MIL-101(Cr), TiO_2/MIL-101(Cr), and Pd/MIL-101(Cr), with the aim of utilizing the high adsorption capability of a MOF material and to study the potential of using this as a DFM for the adsorption and consecutive total destruction of toluene to lesser harmful products such as CO_2 or H_2O. The materials were investigated using conventional surface characterization techniques, and the dynamic adsorption performance along with the conversion of toluene and product yield were analyzed in a fixed bed column with a high aspect ratio. Using further instrumentation techniques, the effect of toluene oxidation on the chemical structure of the DFM was further studied. Our previous works investigated the efficacy of mixed-metal oxides (MMOs) for the same phenomenon;[31,32] however, the uniform dispersion of titania and Pd nanoparticles onto MIL-101(Cr) is hypothesized to provide a much larger conversion potential at lower temperatures, as illustrated in many works done before, as a result of increased number of active sites introduced by the metal/metal oxide incorporation.[43] While the total oxidation process of toluene has been the subject of extensive research,[44] the utilization of a hybrid process for the effective destruction of toluene has seldom been studied.

2. EXPERIMENTAL SECTION

2.1. Materials. All materials were used as received without any further modifications. Chromium nitrate nonahydrate ($Cr(NO_3)3\cdot 9H_2O$), terephthalic acid, nitric acid (HNO_3), titanium(IV) butoxide (TBT), isopropanol, dimethylformamide (DMF), palladium nitrate dihydrate ($Pd(NO_3)_2\cdot 2H_2O$), 1,4-bezenedicarboxylic acid (H_2BDC), and toluene (99%, ACS reagent) were of analytical grade and purchased from Sigma-Aldrich. All gases used in this project were of ultrahigh purity and purchased from Airgas.

2.2. Materials Synthesis. *Synthesis of MIL-101(Cr).* The synthesis method followed was a slightly modified procedure used by Zhao et al.[45] Briefly, about 800 mg of $Cr(NO_3)_3\cdot 9H_2O$ and 328 mg of H_2BDC were mixed together, and subsequently, 180 mg of HNO_3 was added to the mixture. The reactants were mixed and sonicated until a homogeneous solution was obtained. The solution

https://doi.org/10.1021/acs.energyfuels.1c01950
Energy Fuels XXXX, XXX, XXX−XXX

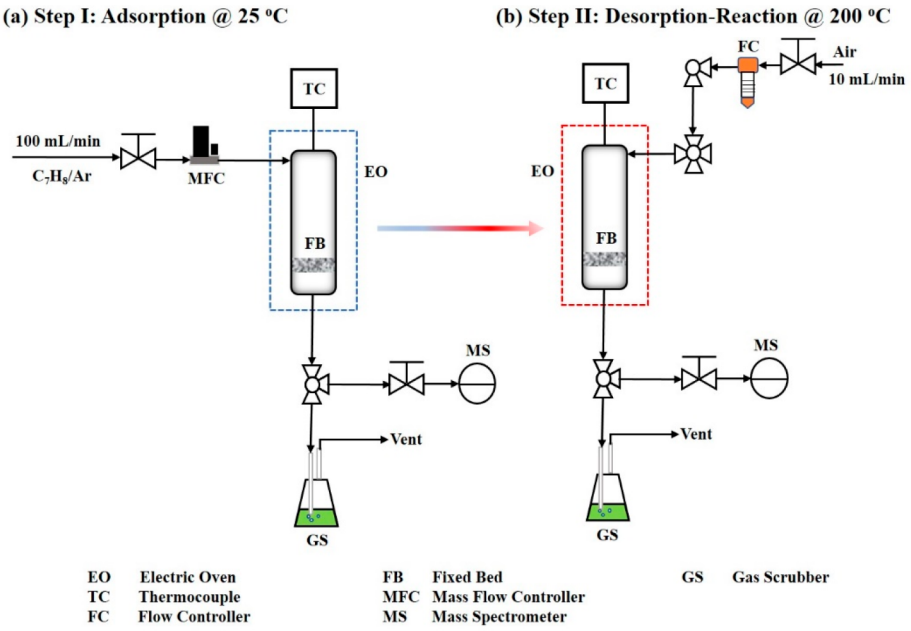

Figure 1. Schematic of the single-column hybrid adsorption catalytic oxidation experiment for (a) adsorption at 25 °C and 1 atm and (b) desorption reaction at 200 °C and 1 atm.

was transferred to an autoclave and kept at 220 °C for 8 h. The material was then cooled, filtered, and solvent exchanged. The obtained solid was washed with DMF and deionized (DI) water and then refluxed in hot ethanol at 70 °C for 5 h.

Synthesis of Pd/MIL-101(Cr). Palladium doped onto MIL-101(Cr) was achieved by using a synthesis procedure mentioned by Qin et al.[26] Here, 500 mg of activated MIL-101(Cr) was dispersed in DMF (10 mL) and stirred for 30 min at room temperature. Then, 13.5 mg of $Pd(NO_3)_2{\cdot}2H_2O$ was mixed with a DMF solution (1 mL). $Pd(NO_3)_2{\cdot}2H_2O$ was added dropwise under vigorous agitation for about 10 min. Shortly after, ultrasonication was performed for 20 min followed by magnetic stirring at room temperature for 24 h. The impregnated solution was then washed with DMF until it turned colorless. Drying was done at lab ambient conditions for 24 h to obtain $PdCl_2$ /MIL-101. To obtain Pd/MIL-101(Cr), the sample was treated at 200 °C for 2 h under an H_2 atmosphere, followed by drying the Pd/MIL-101(Cr) in air for 8 h. The obtained powders are named Pd/MIL-101(Cr).

Synthesis of TiO_2/MIL-101(Cr). Titania was immobilized onto MIL-101(Cr) using a procedure used by Hu et al.[25] Mil-101(Cr) powder (200 mg) was taken and dispersed in isopropanol (65 mL). TBT (50 mL) was added next, and the solution was mixed thoroughly using ultrasonication for 30 min to obtain a highly dispersed phase. The mixture was further subjected to magnetic stirring for 10 h. After centrifugation, the precipitate obtained was washed with isopropanol and left to dry for 48 h. The obtained powder was transferred to an autoclave with 100 mL of ultrapure water. The autoclave was heated to 150 °C and maintained at this temperature for 10 h. On cooling, the mixture was washed with water and left to dry at 80 °C for 12 h. The obtained powders are named TiO_2/MIL-101(Cr).

2.3. Materials Characterization. X-ray diffraction (XRD) was obtained using a PANalytical X'Pert multipurpose X-ray diffractometer. The crystal structure was determined using these results. Bare MIL-101(Cr) was compared to a simulated pattern obtained from the open crystal database to confirm the synthesized structure. Scanning electron microscopy (SEM) was used to investigate the structural morphology of the materials. This was performed using a Hitachi model S4700 field-emission SEM instrument. X-ray photoelectron spectroscopy (XPS) was obtained using a Kratos Axis 165 photoelectron spectrometer using an aluminum X-ray source to excite the samples. Surface characterization was assessed using N_2 physisorption isotherms obtained using a Micromeritics 3Flex gas analyzer at 77 K. Outgassing in a Micromeritics SSmart VaPrep was performed at 120 °C for 6 h. The surface area was consequently determined using the Brunauer–Emmett–Teller (BET) technique, while pore volume was estimated at $P/P_0 = 0.9$. Pore size distribution (PSD) profiles were determined using a non-local density functional theory (NLDFT).

2.4. Adsorption Isotherm Measurements. Equilibrium adsorption experiments were carried out on the samples using a volumetric method. The experiments were carried out at 25 °C and measurements taken over a relative pressure (P/P_0) range of 0–1 on a 3Flex Micromeritics gas analyzer. The toluene vapor used was generated from liquid toluene at 25 °C and 1 atm and was thereafter purified to remove any trapped vapor and gas impurities and subsequently vaporized at 25 °C using the freeze–thaw purification method described elsewhere.[46] A water bath kept at 25 °C was used to maintain the liquid toluene reservoir at a constant temperature of 25 °C throughout the duration of the experiments. In each experiment, about 100 mg of sample was degassed on the Micromeritics Smart VacPrep at 250 °C under vacuum for 6 h and then cooled to 25 °C, before being transferred to the Micromeritics 3Flex for the isotherm measurement.

2.5. Dynamic Adsorption Experiments. The dynamic adsorption capacity of the samples was assessed by breakthrough measurements at 25 °C and 1 atm and up to saturation, i.e., 100% breakthrough in a stainless-steel lab-built column setup depicted in Figure 1a. The column was situated inside a tubular furnace equipped with a PID temperature controller. The type-K thermocouple used to measure and control the furnace temperature was in contact with the reactor wall; however, a temperature difference of about 2 °C was still observed between the furnace and the reactor wall. For each experiment, about 0.2 g of a sample was loaded into the column (see Figure S1 for loading clarification). The vertical reactor was packed bottom-up in the following order: flat wire disk, 1 cm height of quartz beads, 1 cm height of pressed quartz wool, and finally ca. 0.2 g of the DFM. The loaded sample was then degassed *in situ* by ramping the bed temperature from 25 to 120 °C at 10 °C/min and holding at this temperature for 2 h under a 40 mL/min Ar flow. Thereafter, the column was cooled to the adsorption temperature followed by temperature stabilization for about 15 min. At this junction, the bed pores and voids were already saturated with Ar. The gas outlet stream was measured online using a mass spectrometer (BELMass). Thereafter, a 500 ppm_v toluene, balanced in Ar, was continuously

https://doi.org/10.1021/acs.energyfuels.1c01950
Energy Fuels XXXX, XXX, XXX–XXX

fed to the column at 25 °C, 1 atm, and a total flow rate of 100 mL/min, while the column outlet concentration was continuously analyzed online. The bed temperature was continuously recorded using a type-K thermocouple inserted axially with the tip at the center of the bed. Only one thermocouple was used for these experiments because the length of the bed was really small, as small as 2 cm. The flow rates of the setup were monitored by mass flow controllers, while the adsorption temperature was controlled by a K-type thermocouple and a benchtop controller. The flow rate of the bed outlet streamwas measured with a mass flow meter and corrected based on the feed composition.

2.6. Sequential Capture−Destruction Experiments. The DFMs were assessed for their toluene adsorption and oxidation capabilities in sequential capture−destruction tests. For these experiments, the adsorption step was carried out only up to a 5% breakthrough (equivalent ot 25 ppm_v of toluene). This was done in order to not act counterproductive to the sole objective of VOC abatement. For the 5% breakthrough experiments carried out here, the bed outlet stream was analyzed for C_7H_8 as was done during the up-to-saturation (100% breakthrough) dynamic adsorption experiments but was analyzed for C_7H_8, CO_2, H_2O, and possible partial oxidation products (CO, H_2, and C_6H_6) during the subsequent desorption/oxidation step. The weight hourly space velocity (WHSV) used relative to the oxidant air (21%−O_2/79%−N_2) was ca. 1185 h^{-1}. This small value was used to limit possible toluene thermal runaway. For the experiments carried out here, dynamic adsorption of toluene was first performed as described earlier but only up to a 5% breakthrough using the setup depicted in Figure 1a, and the bed outlet feed was analyzed for C_7H_8. At the attainment of the 5% breakthrough, the process was switched from adsorption to desorption/oxidation (Figure 1b) by first closing the VOC streamline, while at the same time opening the 21%−O_2/79%−N_2 oxidant line. The bed temperature was simultaneously ramped from the adsorption temperature of 25 °C to oxidation temperature of 200 °C at 10 °C/min. The reaction was then left to proceed at this temperature until the detection of toluene at the exit of the bed was effectively zero. Both streams used during the 5% breakthrough adsorption and the subsequent desorption/oxidation were fed downwardly toward the inlet of the column. Dynamic data acquisition was performed using a Microtrac BELmass mass spectrometer that was earlier used.

3. RESULTS AND DISCUSSION

3.1. Materials Characterization. Figure 2 illustrates the powder XRD pattern obtained for MIL-101(Cr) and its doped variants. The pattern for the MIL-101(Cr) sample matched well with the so-far published XRD patterns with the main peaks within the investigated range of 2θ (7°−40°) at 2θ = 8.5°, 9.1°, 10.5°, and 16.5° and indexed as planes (822), (753), (666), and (822), respectively.[26] This pattern is identical to the simulated pattern obtained from the crystal database other than the intensity of the peaks being less pronounced in the synthesized MIL-101(Cr). In the case of Pd/MIL-101(Cr), a peak indexed as (111) was obtained at 2θ = 37.5°, though the structure of MIL-101(Cr) was maintained regardless of Pd loading, which was to be expected due to the fairly small loading of Pd onto the MOF. This can also be explained due to the high dispersion of Pd nanoparticles throughout the MOF matrix, an observation that was previously detected in similar compounds.[26] This is also indicative of the small size of the Pd particles deposited on the surface. In the case of the titania-doped sample, a prominent broad diffraction peak was detected around 2θ = 25.2°, which corresponds to (101) indexing in anatase TiO_2.[25] This showed that titania was successfully incorporated into the parent MIL-101 (Cr). The broadness of this peak is an indication of the small sizes of the titania particles according to the Scherrer equation. The smaller the sizes of the nanoparticles doped on the parent MIL-101(Cr) are, the broader or less noticeable the peaks relative to the nanoparticles appeared. Hence, comparing Pd/MIL-101(Cr) and TiO_2/MIL-101(Cr), this means that the Pd nanoparticles were smaller than the titania nanoparticles as was further established via SEM, TEM, N_2 physisorption, and XPS.

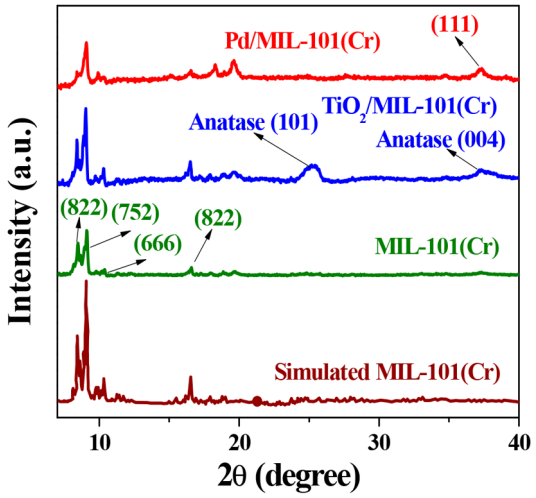

Figure 2. XRD patterns for MIL-101(Cr), TiO_2/MIL-101(Cr), and Pd/MIL-101(Cr).

Figure 3 illustrates the exterior surface morphology of the MOFs synthesized. Figure 3a depicts the STEM image of MIL-101(Cr). Typical octahedral shapes of MIL-101(Cr) crystals were detected with an average size of about 200 nm, in agreement with several previous studies.[47] Figure 3b represents the STEM image of Pd/MIL-101(Cr). What was immediately noticeable was the dispersion of Pd nanoparticles on the surface of the parent MIL-101(Cr) and the relatively smaller crystal sizes (ca. 150 nm). The Pd nanoparticles were about 8 nm in size. Similarly, the dispersion of TiO_2 on MIL-101(Cr) was apparent in Figure 3c; however, the resultant crystals were about 100 nm in size, while the TiO_2 nanoparticles were about

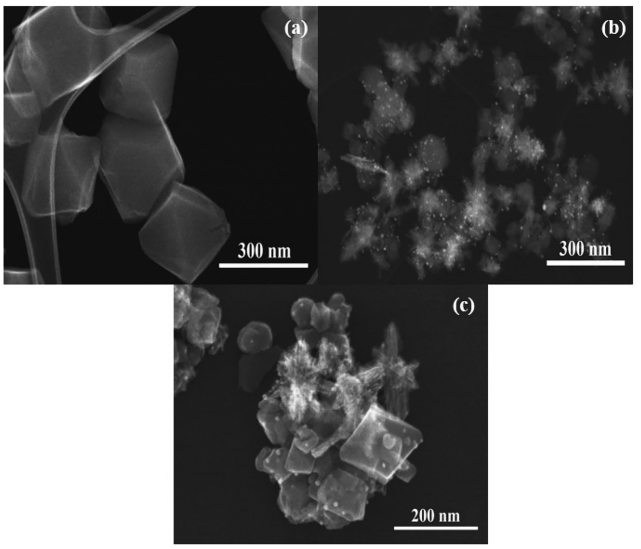

Figure 3. STEM image of (a) MIL-101(Cr), (b) TiO_2/MIL-101(Cr), and (c) Pd/MIL-101(Cr).

https://doi.org/10.1021/acs.energyfuels.1c01950
Energy Fuels XXXX, XXX, XXX−XXX

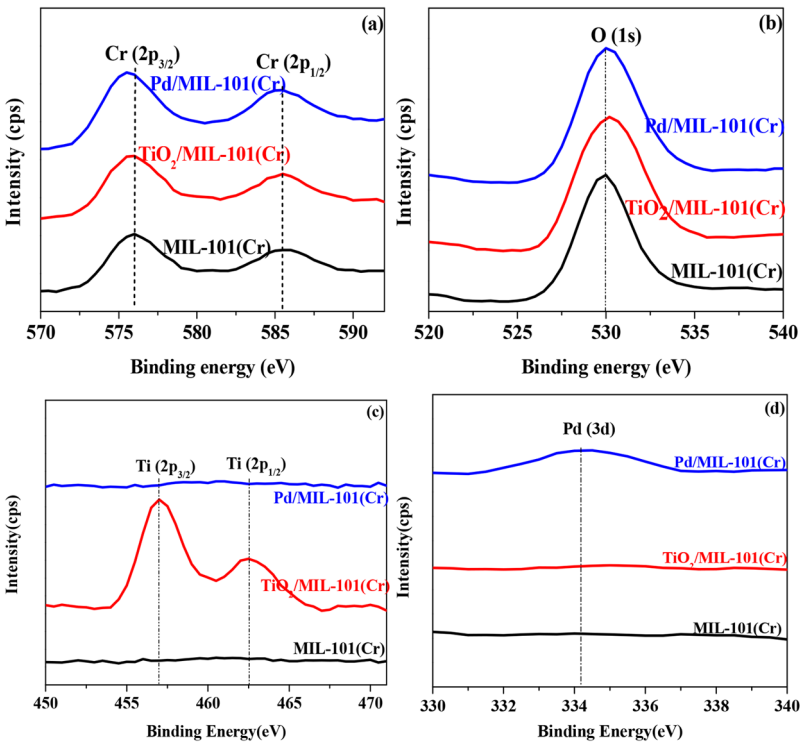

Figure 4. High-resolution XPS spectra of (a) chromium, (b) oxygen, (c) titanium, and (d) palladium.

10 nm in size. Compared to the parent MIL-101(Cr), we noticed a higher rate of agglomeration in distorted crystal shapes in the doped materials. While Pd/MIL-101(Cr) maintained the octahedral shape of its parent MIL-101(Cr), a large shape distortion was observed in the case of TiO_2/MIL-101(Cr). The more regular shape of the former could explain its superior surface properties when compared to the latter.

Figure 4 illustrates the XPS spectra obtained for MIL-101(Cr) and its doped counterparts. The NIST XPS database was used to identify the atomic hybridization of the metal used. Carbon was not represented here due to its association with the instrument used in this measurement. All materials showed Cr $2p_{3/2}$ and $2p_{1/2}$ at 576 and 586 eV, respectively, an atomic splitting of the Cr atom in coordination with the other species in the catalyst (Figure 4a). The doped materials showed a slightly larger Cr peak area, which suggests that the interactions of the Pd and TiO_2 particles with MIL-101 (Cr) were not on the Cr sites. As expected, TiO_2 showed a superior peak area at O 1s at 530 eV (Figure 4b). Since this corresponds to lattice oxygen,[48] we could assume that TiO_2 is present within the lattice along with the surface of the parent MOF. This could also explain the very low surface properties detected during BET surface analysis. This spectrum is reflected through the samples, however, most likely due to M−O-C bonds.[49] Furthermore, the atomic orbital splitting of Ti 2p to Ti $2p_{3/2}$ and $2p_{1/2}$ reveals the state of Ti (Figure 4c) in the form of an oxide, which was similar to what we have observed in our previous work.[50] This illustrates the presence of TiO_2 on MIL-101(Cr) and further explains that the larger area under O 1s for TiO_2/MIL-101(Cr) when compared to the other samples. Pd was observed with a small spectrum obtained at approximately 335 eV (Figure 4d), which corresponds to the 3d atomic distribution. This suggests that Pd^{2+} was successfully reduced to Pd^0.[26] This confirms the doping of reduced Pd nanoparticles on the MOF and the success of the doping procedure. Furthermore, the Pd^0 was detected in only the Pd/MIL-101(Cr) sample. Due to the small loading of Pd, the area under the spectrum was quantitatively inferior to other elements detected, which also explains the superior surface properties of Pd/MIL-101(Cr) when compared to TiO_2/MIL-101(Cr). Furthermore, it is observable that the carboxylate O 1s peak shifted by about 0.9 eV in Pd/MIL-101(Cr) and 1.1 eV in TiO_2/MIL-101(Cr) to higher binding energy with respect to the parent MIL-101(Cr), a situation that could be attributed to the interaction of loaded TiO_2 or Pd with the MIL-101(Cr) framework. It is noteworthy to mention that the higher this shift is, the stronger the interaction of the dopant on the support is. In conclusion, the titanium-, palladium-, chromium-, carbon-, and oxygen-related peaks were all detected in the XPS survey spectra, thereby indicating successful impregnation of TiO_2 or Pd into the parent MIL-101(Cr).

The quantification report, showing the materials' surface mass (%) elemental compositions, derived from the XPS data is represented in Table 1. Clearly, the mass % of Cr in all the materials are similar, thereby showing uniformity in the composition of the bare MIL-101(Cr) in the materials. As expected, the mass % values of O in MIL-101(Cr) and Pd/MIL-101(Cr) are similar, while the amount in TiO_2/MIL-101(Cr) is significantly different. TiO_2 loading into TiO_2/

Table 1. Quantification of Elements Present in Materials from XPS Analysis

	Mass concentration (%)			
Sample	Cr	O	Ti	Pd
MIL-101(Cr)	18.7	32.6	–	–
TiO_2/MIL-101(Cr)	20.1	37.3	18.0	–
Pd/MIL-101(Cr)	21.6	31.7	–	0.7

https://doi.org/10.1021/acs.energyfuels.1c01950
Energy Fuels XXXX, XXX, XXX−XXX

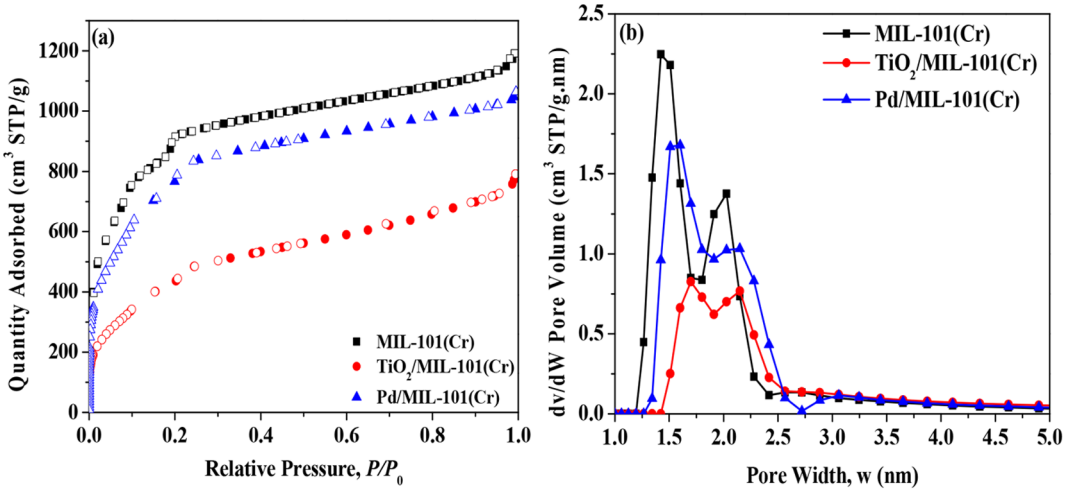

Figure 5. (a) N_2 physisorption isotherms and (b) PSD profiles for bare MIL-101(Cr), TiO_2/MIL-101(Cr), and Pd/MIL-101(Cr).

MIL-101(Cr) was about 18 mass %, while the Pd loading into Pd/MIL-101(Cr) was about 0.7 mass %.

The results of the N_2 physisorption measurements carried out on the materials at −196 °C are shown in Figure 5. According to the IUPAC nomenclature, we could see from Figure 5a that all the materials depicted a type-I isotherm Moreover, two secondary uptakes (at P/P_0 ca. 0.1 and 0.2) indicating two kinds of microporous windows (pentagonal and hexagonal) exist in the MIL-101(Cr) sample.[51] This class of isotherm demonstrates that adsorption occurs on the surface of materials, or monolayer adsorption occurs due to a strong interaction between the adsorbent and the adsorptive. Moreover, the degree of mesoporosity of the materials is small or even negligible, and little or no hysteresis was observed, implying that VOCs adsorption on these materials could be easily reversed via pressure swing. As expected, the amount of N_2 adsorbed decreased as the bare material was doped, with a larger observed drop illustrated by TiO_2/MIL-101(Cr). From the PSD profiles (Figure 5b), we could see that all the materials are bimodal, albeit largely microporous with a small degree of mesoporosity. Moreover, we could see right-bound shifts in PSD as TiO_2 or Pd particles were being impregnated onto the parent MIL-101(Cr). These gradual shifts in PSD were attributed to the partial blockage of the pores as TiO_2 or Pd nanoparticles were being impregnated onto the bare MIL-101(Cr). It is noticeable that the shift due to TiO_2 loading was higher than that due to Pd loading. This observation is most certainly due to two factors, namely, the amount of loading and the size of the loaded particles. This served as another evidence that the amount and/or size of TiO_2 loaded onto the MIL-101(Cr) was higher than that of the Pd, as was earlier suggested by SEM, TEM, and XPS.

The materials' surface characteristics (surface area, pore volume, and pore size) determined from the N_2 physisorption isotherms are shown in Table 2. The parent MIL-101(Cr), with a S_{BET} = 3273 m^2/g, suffered about a 10% reduction in surface area when doped with Pd and a whopping 50% loss due to TiO_2 doping. The total pore volume, V_{tot}, followed a similar trend with ca. 10% and 35% losses due to Pd and TiO_2 loadings, respectively. A more severe loss with TiO_2 was certainly due to its higher loading amount (18 wt % against 0.7 wt %). Typically, this loss in surface properties has been attributed to pore blockage caused by the loading of Pd and

Table 2. Textural Properties of MIL-101(Cr) and Its Doped Counterparts

Sample	S_{BET} (m^2/g)	V_{tot} (cm^3/g)	$V\mu$ (cm^3/g)	d_p (nm)	$V\mu/V_{tot}$
MIL-101(Cr)	3273	1.76	1.05	1.4, 1.9	0.60
TiO_2/MIL-101(Cr)	1698	1.13	0.37	1.6, 2.1	0.33
Pd/MIL-101(Cr)	2936	1.59	0.82	1.8, 2.3	0.52

TiO_2 nanoparticles. The bare MIL-101(Cr) depicted a largely microporous PSD with modal pore diameters, d_p, of 1.4 and 1.9 nm, in contrast to the doped materials, which suggested a change in the pore system, 1.6 and 2.1 nm for TiO_2/MIL-101(Cr) and 1.7 and 2.2 nm for Pd/MIL-101(Cr). The kinetic diameter of toluene is 0.59 nm, much smaller than the measured pore sizes.[52] Hence, although the impregnation of MIL-101(Cr) with TiO_2 or Pd decreased the surface area and pore volume, the pores were still maintained and accessible to toluene molecules, thus facilitating the diffusion and adsorption of toluene molecules.

3.2. Toluene Vapor Adsorption Isotherms. Figure 6 shows the toluene vapor adsorption isotherms obtained for the

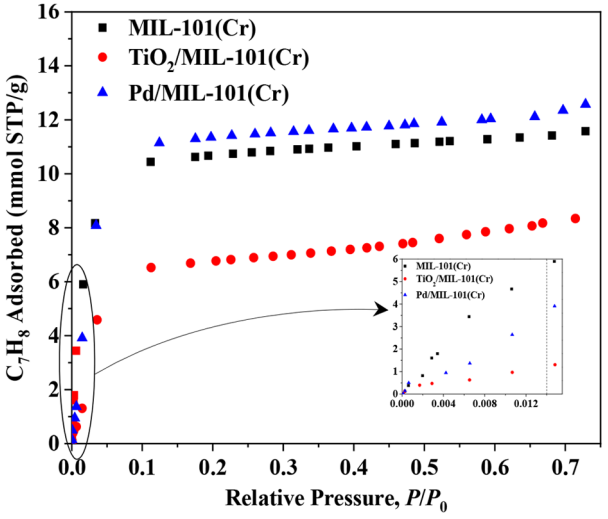

Figure 6. Toluene adsorption isotherms for three samples at 25 °C and pressure up to toluene saturation pressure.

https://doi.org/10.1021/acs.energyfuels.1c01950
Energy Fuels XXXX, XXX, XXX−XXX

three samples. The inset therein contains the isotherms in the low-pressure range that covers the toluene bed inlet pressure ($P/P_0 \approx 0.014$) used during the dynamic adsorption experiments. Notably, all the isotherms were of type-I based on the IUPAC classification, implying that the materials were largely microporous and are sorption reversible.[53] In the low-pressure region (shown in the inset), the toluene uptake increased in the order of TiO_2/MIL-101(Cr) < Pd/MIL-101(Cr) < MIL-101(Cr) as a function of the surface area and pore volume of the materials, shown in Table 2. Here, the equilibrium uptake of MIL-101(Cr) was about twice that of Pd/MIL-101(Cr). However, as the pressure approached the toluene saturation vapor pressure, i.e., P/P_0 approaches 1, the equilibrium uptake of the samples rather followed TiO_2/MIL-101(Cr) < MIL-101(Cr) < Pd/MIL-101(Cr), where the capacity of Pd/MIL-101(Cr) was about 10% greater than that of MIL-101(Cr). The higher toluene uptake of Pd/MIL-101(Cr) relative to MIL-101(Cr) at higher pressures could be attributed to metal−π interactions between Pd and toluene.[26] However, the lower uptake over Pd/MIL-101(Cr) in the low-pressure region compared to MIL-101(Cr) suggests that π-complexation might be pressure dependent. Going by Figure 6, the materials were essentially homogeneous, implying that only one type of surface was responsible for adsorption thereon.

3.3. Dynamic Adsorption Profiles. The results of the toluene dynamic adsorption experiments carried out on the samples up to a 100% breakthrough are shown in Figure 7. The

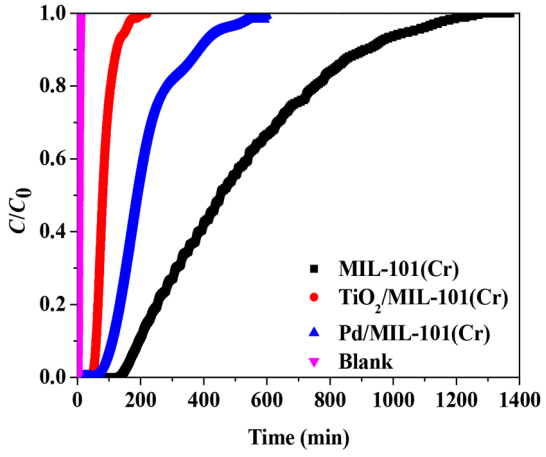

Figure 7. Toluene breakthrough profiles over MIL-101(Cr) and its doped variants. Experimental conditions: 500 ppm_v C_7H_8 in Ar, 100 mL (STP)/min, 25 °C, and 1 atm.

blank run result was included to show the hydrodynamics of an empty column. After initial degassing of the bed at 250 °C for 2 h under a 40 mL/min flow of Ar and subsequent cooling and stabilization at 25 °C, constant 500 ppm_v toluene in Ar was fed into the bed at 1 atm and 100 mL/min. The response to the feed concentration step perturbation created a mass transfer zone that propagated through the bed at a rate determined by equilibrium. As expected, while toluene was being adsorbed on the materials, it was not detected at the bed outlet, and only when the breakthrough times were reached was toluene detected in the exit gas stream. Toluene breakthrough was defined as the point where the toluene bed outlet concentration was 5% of its inlet concentration. Clearly, the toluene 5% breakthrough time ($t_{0.05}$) at the outlet of the bed occurred in the order of TiO_2/MIL-101(Cr) < Pd/MIL-101(Cr) < MIL-101(Cr). Similarly, the other characteristic time, i.e., $t_s = t_{1.0}$ (time at saturation = time at 100 % breakthrough), followed accordingly. This trend could be ascribed to the surface area and the pore volume.[54] Also observable is the steepness of the curves. The mass and heat transfer resistances within particles and the bed have been reported to be responsible for the shape of the breakthrough curves. However, in this study, because of the low concentration of toluene in the feed, the effect of heat transfer resistance on the broadness was negligible and thus led to the conclusion that only the mass transfer resistance was responsible for the broad fronts observed therein.[55] From the SEM and TEM images in Figure 3, we could see that the sizes of the particles were in the order of TiO_2/MIL-101(Cr) < Pd/MIL-101(Cr) < MIL-101(Cr), thereby resulting in short diffusion path length. This result agreed with the N_2 adsorption results and similarly the toluene equilibrium adsorption results at the relative pressure that corresponded to the dynamic experiments toluene partial pressure.

The values of the key parameters, calculated from the results of the dynamic adsorption experiments in conjunction with eqs S1 and S2 in the Supporting Information, are presented in Table 3. The toluene equilibrium adsorption capacities of the samples at the relative pressure that corresponded with the bed inlet toluene concentration during the breakthrough experiments were also included in this table for comparison. It is worth mentioning that the characteristic time values, i.e., $t_{0.05}$ and t_s related to the blank run, were subtracted from the corresponding raw time values related to the samples to arrive at the actual characteristic time values for the samples. As revealed in the table, MIL-101(Cr) showed the longest $t_{0.05}$, followed by Pd/MIL-101(Cr) and then TiO_2/MIL-101(Cr). A similar trend was also observed in t_s. A similar trend was also observed at 50% and 100% C_7H_8 breakthrough levels for all the samples. Consequently, MIL-101(Cr) had the highest dynamic adsorption capacity of C_7H_8 at all breakthrough levels (1.7and 5.1 mmol/g, respectively, at 5% and 100% breakthrough levels), followed by Pd/MIL-101(Cr) (0.9 and 3.2 mmol/g) and then TiO_2/MIL-101(Cr) (0.6 and 0.9 mmol/g). These observations were in agreement with the progressive change in textural and surface properties shown in Table 2 and have been similarly reported by Ncube et al.[56] As expected, the dynamic adsorption capacities ($q_{d,s}$) were not significantly different from the equilibrium adsorption capacities ($q_{eq@p/p0=0.014}$). The dynamic adsorption capacity is often less than the static adsorption capacity due to the effect of flow axial dispersion and backmixing which often hinder the

Table 3. Dynamic Adsorption Data Obtained from Breakthrough Profiles

Sample	$t_{0.05}$ (min)	t_s (min)	$q_{d,0.05}$ (mmol/g)	$q_{d,s}$ (mmol/g)	$q_{eq@p/p0=0.014}$ (mmol/g)
MIL-101(Cr)	168	506	1.7	5.1	5.6
TiO_2/MIL-101(Cr)	55	84	0.6	0.9	1.2
Pd/MIL-101(Cr)	90	211	0.9	3.2	3.6

https://doi.org/10.1021/acs.energyfuels.1c01950
Energy Fuels XXXX, XXX, XXX−XXX

Table 4. Materials' Performance Comparison Based on Partition Coefficients (PC)

Sample	$t_{0.05}$ (min)	$q_{d,0.05}$ (mmol/g)	$PC_{0.05}$ (mol/kg/Pa)	t_s (min)	$q_{d,s}$ (mmol/g)	PC_s (mol/kg/Pa)
MIL-101(Cr)	168	1.7	0.67	506	5.1	0.11
TiO_2/MIL-101(Cr)	55	0.6	0.24	84	0.9	0.02
Pd/MIL-101(Cr)	90	0.9	0.36	211	3.2	0.07

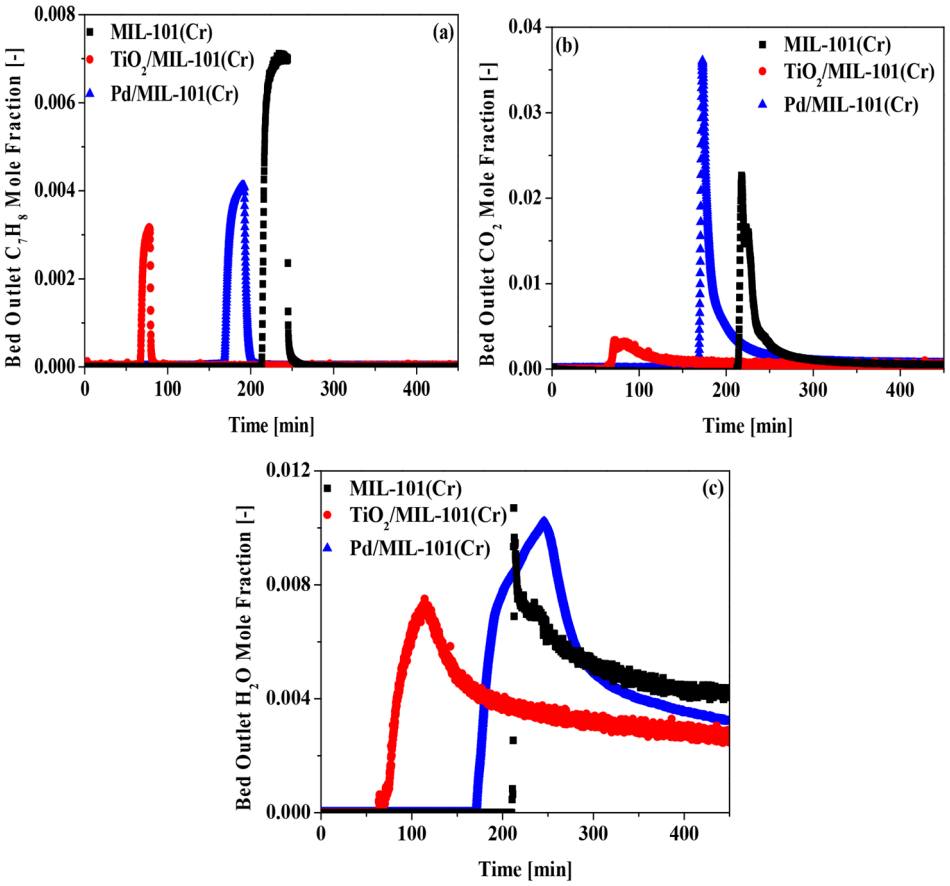

Figure 8. Bed outlet concentration profiles for (a) thermal runaway of C_7H_8 and evolved (b) CO_2 and (c) H_2O. Adsorption: 500 ppm_v C_7H_8 in Ar, 100 mL (STP)/min, 25 °C, and 1 atm. Desorption/oxidation: 21% O_2−79% N_2, 10 mL (STP)/min, 25−250 °C, and 1 atm.

attainment of equilibrium during dynamic adsorption.[57] The dynamic adsorption capacity might be in the range of ∼25%−70% of the equilibrium adsorption capacity.

The partition coefficient (PC) was used to quantitaitively compare the adsorption performance of the materials investigated in this study to those of other materials for toluene adsorption without any bias. The PC values were calculated using eq S3 in the Supporting Information. Shown in Table 4 are the PC values of the materials investigated in this study at different breakthrough levels. Each corresponding dynamic adsorption capacity was also included for comparison. At the 5% breakthrough level, MIL-101(Cr), TiO_2/MIL-101(Cr), and Pd/MIL-101(Cr) had PC values of 0.67, 0.24, and 0.36 mol/kg/Pa, respectively, while at the 100% breakthrough the values were 0.11, 0.02, and 0.07 mol/kg/Pa, respectively. The trends observed herein agreed with the adsorption capacity trends as well as the textural properties discussed earlier. Kim et al.[58] in their review paper compared PC values of about 100 adsorbents conventionally used for toluene abatement. From the report, we could establish that the PC values of MIL-101(Cr) and its variants investigated in this study were higher than almost 50% of those reported therein, suggesting that our materials are competitive for toluene adsorption. Moreover, it should also be noted that the materials in this study were investigated for their adsorbent/catalyst dual functionality.

3.4. Sequential Capture−Destruction Performances.

In Section 3.3, the toluene dynamic adsorption capacities of the DFMs were determined via breakthrough experiments. Although these runs provided vital information about the adsorption properties of the materials, a one-bed−one-column reactor, as in this investigation, cannot be operated till saturation unless the material of interest has a very thin mass transfer zone (MTZ), i.e., high mass transfer coefficient, for this would amount to emitting a significant portion of the toluene throughput back to the atmosphere resulting in a counterproductive endeavor. So, oftentimes, adsorption is usually ended when a given threshold, corresponding to an environmentally permissible level of VOC emission, is reached at the bed outlet. For this reason, the dynamic adsorption step of the sequential adsorption reaction runs was only carried out till 5% toluene breakthrough (25 ppm_v) was attained after which desorption/oxidation was initiated. Shown in Figure 8 are the results of the temperature swing desorption/oxidation

https://doi.org/10.1021/acs.energyfuels.1c01950
Energy Fuels XXXX, XXX, XXX−XXX

experiments. It should be noted that the transition from adsorption to desorption/oxidation took place at ca. 215, 65, 165 min, respectively, for MIL-101(Cr), TiO_2/MIL-101(Cr), and Pd/MIL-101(Cr). The temperature profiles are shown in Figure S1 in the Supporting Information. From Figure S1, it is evident that the light-off temperature was similar and about 187 °C, resulting in a slightly exothermic oxidation reaction. This was not unexpected given the low adsorbate saturation (5%) and the low regenerative O_2 flow rate (10 mL/min) used for these experiments.[36] When the bed temperature was still below the catalytic oxidation temperature, most of the desorbed toluene escaped out of the bed due to toluene thermal runaway/excursion, reflected as the roll-ups in Figure 8a. The magnitude of the roll-up originated from two contributions: first from C_7H_8 in the materials pores and voids of the bed at the end of adsorption, and then from desorbed but unoxidized C_7H_8. The thermal runaway of desorbed and unreacted VOCs is a major determinant of the efficacy of any material for VOCs conversion into benign products (CO_2 and H_2O).[36] From Figure 8a, it is evident that toluene thermal runaway increased in the order of the adsorption capacity of the materials, that is, MIL-101(Cr) > Pd/MIL-101(Cr) > TiO_2/MIL-101(Cr). During the desorption/oxidation step, the thermal runaway occurred in the first 40, 20, and 30 min, respectively, for the samples, until the light-off took place. Hence, we could conclude that the higher the 5% breakthrough adsorption capacity of the materials is, the higher is the toluene thermal runaway and thus the lower the conversion. This is in accordance with the results that reported by various authors.[36,37] Among all the materials, the main reaction products were CO_2 and H_2O. The yields of CO_2 and H_2O were found to be in the order of Pd/MIL-101(Cr) > MIL-101(Cr) > TiO_2/MIL-101(Cr). It is imperative to mention here that CO was not produced during the reaction, but some amounts of H_2 and C_6H_6 were produced as a result of partial oxidation of the desorbed toluene (Figure S2, Supporting Information). From Figure 8b, based on the steepness of the curves and the area under the curves, it is conclusive that Pd/MIL-101(Cr) possessed high catalytic activity and high yield formation, followed by the parent MIL-101(Cr). However, from Figure 8c, it is clear that TiO_2/MIL-101(Cr) produced the smallest amount of benzene throughout the entire reaction period, while MIL-101(Cr) produced the largest. This again was in agreement with the adsorbate loading of the materials at 5% saturation. Moreover, the maximum quantities of benzene produced by MIL-101(Cr) and Pd/MIL-101(Cr) were reached within 30 min of the reaction. Benzene formation occurred before the light-off phenomenon for MIL-101(Cr) and TiO_2/MIL-101(Cr) most probably via a C_7H_8 disproportionation reaction but after for Pd/MIL-101(Cr) via thermal decomposition.[36]

Table 5 depicts the summary of the process's key performance indicators, calculated using eqs S4−S12 in the Supporting Information. With MIL-101(Cr) having the least C_7H_8 overall conversion at 76%, TiO_2/MIL-101(Cr) and Pd/MIL-101(Cr) were about 16% and 6% higher, respectively. A number of factors could be responsible for this. On the one hand, the high conversion of TiO_2/MIL-101(Cr) relative to the other two samples could be related to its high lattice oxygen content as shown in Table 1. This suggests that the oxidation mechanism in TiO_2/MIL-101(Cr) followed the Mars−van Kreven (MVK) model. On the other hand, this could also be due to its low adsorbate loading. At low adsorbate loading, thermal runaway is usually low, thus increasing conversion.[36] Also, this could be due to its relatively large pore diameter. The large pore diameter could facilitate the transfer of the oxidant molecules to the catalytic active sites, as reported by earlier researchers.[35,37] However, it should be mentioned that this was less likely since the pore diameters were not significantly different as shown in Table 1. Finally, we could attribute this to the small particle size of the material as shown in Figure 3. The small particle size with a short diffusion path length could facilitate faster transfer of the oxidant to the catalytic active sites. Due to the formation of byproducts (C_6H_6 and H_2) via partial oxidation, the destruction to benign CO_2 and H_2O was lower than the overall conversion, as shown in Table 5. It should be mentioned that this is however unwanted and thus requires the process design and operating conditions to be optimized to ensure complete combustion. Generally, for adsorbent−catalyst DFMs, the most appropriate measure of catalytic activity is the turnover frequency (TOF) because it takes into consideration the fact that only a portion of the materials and the active sites thereon is available for catalysis, thus allowing performance assessment by considering both the strength of and the number of catalyst active sites on the materials. On the basis of this, and as explained in the Supporting Information, the reaction TOF values of the materials were calculated, and the results are included in Table 5. Pd/MIL-101(Cr) exhibited the highest TOF value at 1.32 $mol_{C7H8}/mol_{AS}/s$, which was about 13% and 8% higher than those of Pd/MIL-101(Cr) and TiO_2/MIL-101(Cr), respectively. It is important to mention that although TiO_2/MIL-101(Cr) had a higher C_7H_8 *in situ* conversion than Pd/MIL-101(Cr), its TOF value was lower primarilydue to its higher loading. The values of the TOF reported in this study are slightly higher than those estimated for other DFMs that have been assessed for sequential adsorption and desorption/oxidation of toluene.[31] However, it should be noted that since both Pd and TiO_2 were physically placed into the pores of the porous MOF host, further cyclic tests are required to fully assess their adsorption−destruction stability and estimate any performance loss over multiple cycles.

Table 5. Toluene Oxidation Performance Variables (Conversion and TOF Values)

Sample	C_7H_8 overall conversion (%)	C_7H_8 conversion to CO_2 and H_2O (%)	Reaction TOF ($mol_{C7H8}/mol_{AS}/s$)
MIL-101(Cr)	76	72	1.15
TiO_2/MIL-101(Cr)	88	80	1.21
Pd/MIL-101(Cr)	80	73	1.32

Fourier-transform infrared spectroscopy of the pyridine-saturated samples (Py-FTIR) and that of the bare samples (FTIR) (as controls) were carried out to determine the contribution of Lewis and Brønsted acid sites to the acidity and thus further probe into the activity comparison of the samples. The results of the analyses are illustrated in Figure 9. As shown in Figure 9a, the major bands observed in the bare MIL-101(Cr) can be seen at 1600, 1400, 1170, 1020, 890, and 590 cm^{-1} in accordance with the work of Haghighi and Zeinali.[59] Moreover, it is interesting that all these bands were preserved in the bare TiO_2/MIL-101(Cr) and Pd/MIL-101(Cr) samples as shown in Figure 9b and c. This revealed that no new chemical functional groups were formed on the surface of MIL-101(Cr) when impregnated with either TiO_2 or Pd; that

https://doi.org/10.1021/acs.energyfuels.1c01950
Energy Fuels XXXX, XXX, XXX−XXX

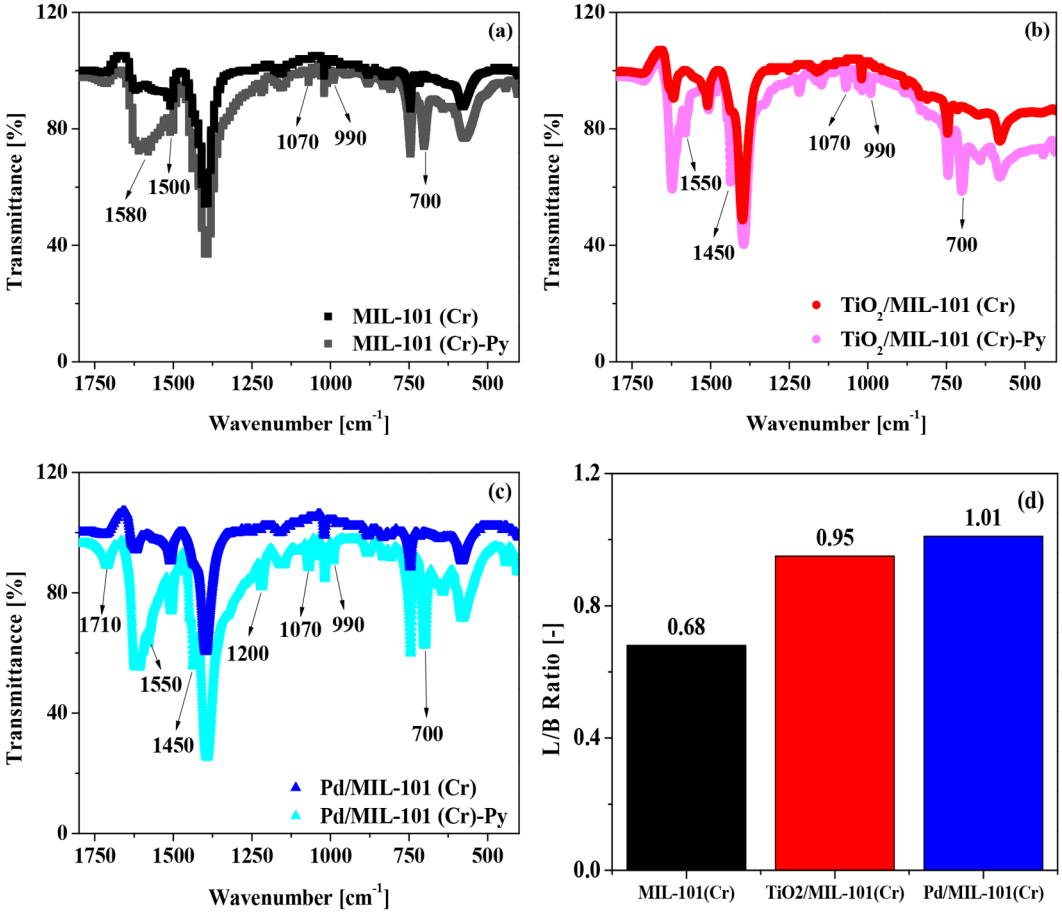

Figure 9. FTIR spectra of pyridine-adsorbed samples (a) MIL-101(Cr), (b) TiO_2/MIL-101(Cr), (c) Pd/MIL-101(Cr), and (d) Lewis to Brønsted acid sites (L/B) concentration ratios.

is, TiO_2 or Pd was only physically bonded. The new bands due to pyridine−acid interaction are the ones annotated in this figure. Those bands common to all the samples are at 700, 990, 1070, 1450−1500, and 1550−1580 cm^{-1}. The bands at 1450−1500 cm^{-1} have been historically attributed to Lewis acid sites and those at 1550−1580 cm^{-1} to Brønsted sites. However, Pd/MIL-101(Cr) formed another prominent acid site at 1710 cm^{-1} due to Pd−pyridine π-interaction.[26] The ratios of the Lewis to Brønsted (L/B) acid sites are shown in Figure 9d. It is evident that Pd/MIL-101(Cr) had a Lewis to Brønsted ratio of 1.01 and TiO_2/MIL-101(Cr) had 0.95, whereas for MIL-101(Cr), this ratio was found to be 0.68. Relating this ratio to the specific catalytic activity (e.g., TOF values) of these materials, we can see that the higher the specific catalytic activity is, the higher the L/B ratio is.

4. CONCLUSIONS

In this study, Pd/MIL-101(Cr) and TiO_2/MIL-101(Cr) were prepared and investigated for adsorption and oxidation of toluene in a combined capture−destruction process along with bare MIL-101(Cr). For the low concentration of VOC (500 ppm_v) tested in this study, MIL-101(Cr) was revealed to have the highest adsorption capacity at 5.6 mmol/g, followed by Pd/MIL-101(Cr) at 3.6 mmol/g and then TiO_2/MIL-101(Cr) at 1.2 mmol/g. Doping of titania resulted in a drastic reduction in toluene uptake, which was due to the reduced surface area available for this process. While a direct relationship between surface properties and uptake was observed for the dilute VOC stream, Pd-doped MIL-101(Cr) illustrated an enhancement in uptake due to further π-interactions in the catalyst system as concentration increased. The combined capture−destruction of VOCs over DFMs, such as the ones investigated in this study, is an intricate process. In general, it includes a rivalry between endothermic desorption and exothermic oxidation of VOCs. Energy is consumed to desorb the already adsorbed VOCs from the internal surface of the DFM and also to raise the temperature of the reactor system to the catalyst operating temperature. The fast temperature increase after light-off heats the bed and subsequently causes desorption of the adsorbed VOC, produces the VOC oxidation threshold concentration, and eventually leads to autothermal oxidation. Pd/MIL-101(Cr) exhibited the highest toluene TOF and Lewis to Brønsted acid sites ratio, and consequently relatively high yields of CO_2 and H_2O when compared to the other materials. This study highlights the potential of Pd/MIL-101(Cr) as an effective DFM for the efficient removal and subsequent destruction of toluene.

■ ASSOCIATED CONTENT

Supporting Information

The Supporting Information is available free of charge at https://pubs.acs.org/doi/10.1021/acs.energyfuels.1c01950.

Reactor temperature profile during temperature swing desorption/oxidation step, bed outlet concentration

https://doi.org/10.1021/acs.energyfuels.1c01950
Energy Fuels XXXX, XXX, XXX−XXX

profiles for evolved C_6H_6, and H_2, and description of dynamic adsorption capacity calculations (PDF)

AUTHOR INFORMATION

Corresponding Author

Fateme Rezaei − *Department of Chemical and Biochemical Engineering, Missouri University of Science and Technology, Rolla, Missouri 65409, United States;* orcid.org/0000-0002-4214-4235; Email: rezaeif@mst.edu

Authors

Busuyi O. Adebayo − *Department of Chemical and Biochemical Engineering, Missouri University of Science and Technology, Rolla, Missouri 65409, United States*

Anirudh Krishnamurthy − *Department of Chemical and Biochemical Engineering, Missouri University of Science and Technology, Rolla, Missouri 65409, United States*

Qasim Al-Naddaf − *Department of Chemical and Biochemical Engineering, Missouri University of Science and Technology, Rolla, Missouri 65409, United States*

Ali A. Rownaghi − *Department of Chemical and Biochemical Engineering, Missouri University of Science and Technology, Rolla, Missouri 65409, United States;* orcid.org/0000-0001-5228-5624

Complete contact information is available at: https://pubs.acs.org/10.1021/acs.energyfuels.1c01950

Notes

The authors declare no competing financial interest.

ACKNOWLEDGMENTS

The authors thank the National Science Foundation (NSF CBET-1802049) for financially supporting this project.

REFERENCES

(1) Gelles, T.; Krishnamurthy, A.; Adebayo, B.; Rownaghi, A.; Rezaei, F. Abatement of Gaseous Volatile Organic Compounds: A Material Perspective. *Catal. Today* **2020**, *350*, 3−18.

(2) Krishnamurthy, A.; Adebayo, B.; Gelles, T.; Rownaghi, A.; Rezaei, F. Abatement of Gaseous Volatile Organic Compounds: A Process Perspective. *Catal. Today* **2020**, *350*, 100−119.

(3) Zhang, G.; Song, A.; Duan, Y.; Zheng, S. Enhanced Photocatalytic Activity of TiO_2/Zeolite Composite for Abatement of Pollutants. *Microporous Mesoporous Mater.* **2018**, *255*, 61−68.

(4) Hu, L.; Cheng, W.; Zhang, W.; Wu, F.; Peng, S.; Li, J. Monolithic Bamboo-Based Activated Carbons for Dynamic Adsorption of Toluene. *J. Porous Mater.* **2017**, *24* (2), 541−549.

(5) Diao, R.; Zhang, H.; Zhao, D.; Li, S. Adsorption and Structure of Benzene, Toluene, and p-Xylene in Carbon Slit Pores: A Monte Carlo Simulation Study. *Chem. Eng. Sci.* **2019**, *197*, 120−134.

(6) Han, M.; Wang, C.; Liu, H. Comparison of Physical Technologies for Biomass Control in Biofilters Treating Gaseous Toluene. *J. Air Waste Manage. Assoc.* **2018**, *68*, 1118−1125.

(7) Everaert, K.; Degreve, J.; Baeyens, J. VOC − Air Separations Using Gas Membranes. *J. Chem. Technol. Biotechnol.* **2003**, *78* (2−3), 294−297.

(8) Quoc An, H. T.; Pham Huu, T.; Le Van, T.; Cormier, J. M.; Khacef, A. Application of Atmospheric Non Thermal Plasma-Catalysis Hybrid System for Air Pollution Control: Toluene Removal. *Catal. Today* **2011**, *176* (1), 474−477.

(9) Bhatt, P. M.; Belmabkhout, Y.; Cadiau, A.; Adil, K.; Shekhah, O.; Shkurenko, A.; Barbour, L. J.; Eddaoudi, M. A Fine-Tuned Fluorinated MOF Addresses the Needs for Trace CO_2 Removal and Air Capture Using Physisorption. *J. Am. Chem. Soc.* **2016**, *138* (29), 9301−9307.

(10) Zhang, X.; Gao, B.; Creamer, A. E.; Cao, C.; Li, Y. Adsorption of VOCs onto Engineered Carbon Materials: A Review. *J. Hazard. Mater.* **2017**, *338*, 102−123.

(11) VanOsdell, D. W.; Owen, M. K.; Jaffe, L. B.; Sparks, L. E. VOC Removal at Low Contaminant Concentrations Using Granular Activated Carbon. *J. Air Waste Manage. Assoc.* **1996**, *46* (9), 883−890.

(12) Mohammed, J.; Nasri, N. S.; Ahmad Zaini, M. A.; Hamza, U. D.; Ani, F. N. Adsorption of Benzene and Toluene onto KOH Activated Coconut Shell Based Carbon Treated with NH_3. *Int. Biodeterior. Biodegrad.* **2015**, *102*, 245−255.

(13) Yu, L.; Wang, L.; Xu, W.; Chen, L.; Fu, M.; Wu, J.; Ye, D. Adsorption of VOCs on Reduced Graphene Oxide. *J. Environ. Sci. (Beijing, China)* **2018**, *67*, 171−178.

(14) Kubo, S.; Kosuge, K. Salt-Induced Formation of Uniform Fiberlike SBA-15 Mesoporous Silica Particles and Application to Toluene Adsorption. *Langmuir* **2007**, *23* (23), 11761−11768.

(15) Ushiki, I.; Ota, M.; Sato, Y.; Inomata, H. VOCs (Acetone, Toluene, and n-Hexane) Adsorption Equilibria on Mesoporous Silica (MCM-41) over a Wide Range of Supercritical Carbon Dioxide Conditions: Experimental and Theoretical Approach by the Dubinin−Astakhov Equation. *Fluid Phase Equilib.* **2015**, *403*, 78−84.

(16) Kim, M.; Ryu, Y.; Lee, C. Adsorption Equilibria of Water Vapor on Activated Carbon and DAY Zeolite. *J. Chem. Eng. Data* **2005**, *50*, 951−955.

(17) Vellingiri, K.; Kumar, P.; Deep, A.; Kim, K. H. Metal-Organic Frameworks for the Adsorption of Gaseous Toluene under Ambient Temperature and Pressure. *Chem. Eng. J.* **2017**, *307*, 1116−1126.

(18) Li, Y.; Miao, J.; Sun, X.; Xiao, J.; Li, Y.; Wang, H.; Xia, Q.; Li, Z. Mechanochemical Synthesis of Cu-BTC@GO with Enhanced Water Stability and Toluene Adsorption Capacity. *Chem. Eng. J.* **2016**, *298*, 191−197.

(19) Barea, E.; Montoro, C.; Navarro, J. A. R. Toxic Gas Removal-Metal-Organic Frameworks for the Capture and Degradation of Toxic Gases and Vapours. *Chem. Soc. Rev.* **2014**, *43*, 5419−5430.

(20) Hong, D. Y.; Hwang, Y. K.; Serre, C.; Férey, G.; Chang, J. S. Porous Chromium Terephthalate MIL-101 with Coordinatively Unsaturated Sites: Surface Functionalization, Encapsulation, Sorption and Catalysis. *Adv. Funct. Mater.* **2009**, *19* (10), 1537−1552.

(21) Xia, Y.; Dai, H.; Jiang, H.; Deng, J.; He, H.; Au, C. T. Mesoporous Chromia with Ordered Three-Dimensional Structures for the Complete Oxidation of Toluene and Ethyl Acetate. *Environ. Sci. Technol.* **2009**, *43* (21), 8355−8360.

(22) Xiao, J.; Li, X.; Deng, S.; Wang, F.; Wang, L. NOx Storage-Reduction over Combined Catalyst $Mn/Ba/Al_2O_3$-$Pt/Ba/Al_2O_3$. *Catal. Commun.* **2008**, *9* (5), 563−567.

(23) Bahri, M.; Haghighat, F.; Kazemian, H.; Rohani, S. A Comparative Study on Metal Organic Frameworks for Indoor Environment Application: Adsorption Evaluation. *Chem. Eng. J.* **2017**, *313*, 711−723.

(24) Shafiei, M.; Alivand, M. S.; Rashidi, A.; Samimi, A.; Mohebbi-Kalhori, D. Synthesis and Adsorption Performance of a Modi Fied Micro-Mesoporous MIL- 101 (Cr) for VOCs Removal at Ambient Conditions. *Chem. Eng. J.* **2018**, *341* (February), 164−174.

(25) Hu, Y.; Huang, Z.; Zhou, L.; Wang, D.; Li, G. Synthesis of Nanoscale Titania Embedded in MIL-101 for the Adsorption and Degradation of Volatile Pollutants with Thermal Desorption Gas Chromatography and Mass Spectrometry Detection. *J. Sep. Sci.* **2014**, *37* (12), 1482−1488.

(26) Qin, W.; Cao, W.; Liu, H.; Li, Z.; Li, Y. Metal-Organic Framework MIL-101 Doped with Palladium for Toluene Adsorption and Hydrogen Storage. *RSC Adv.* **2014**, *4* (5), 2414−2420.

(27) Duyar, M. S.; Treviño, M. A. A.; Farrauto, R. J. Dual Function Materials for CO_2 Capture and Conversion Using Renewable H_2. *Appl. Catal., B* **2015**, *168*−*169*, 370−376.

(28) Al-Mamoori, A.; Rownaghi, A. A. A. A.; Rezaei, F. Combined Capture and Utilization of CO_2 for Syngas Production over Dual-Function Materials. *ACS Sustainable Chem. Eng.* **2018**, *6* (10), 13551−13561.

(29) Al-mamoori, A.; Lawson, S.; Rownaghi, A. A.; Rezaei, F. Oxidative Dehydrogenation of Ethane to Ethylene in an Integrated CO_2 Capture-Utilization Process. *Appl. Catal., B* **2020**, *278* (July), 119329.
(30) Miguel, C. V.; Soria, M. A.; Mendes, A.; Madeira, L. M. A Sorptive Reactor for CO_2 Capture and Conversion to Renewable Methane. *Chem. Eng. J.* **2017**, *322*, 590−602.
(31) Adebayo, B. O.; Krishnamurthy, A.; Rownaghi, A. A.; Rezaei, F. Toluene Abatement by Simultaneous Adsorption and Oxidation over Mixed-Metal Oxides. *Ind. Eng. Chem. Res.* **2020**, *59* (30), 13762−13772.
(32) Adebayo, B. O.; Newport, K.; Yu, H.; Rownaghi, A. A.; Liang, X.; Rezaei, F. Atomic Layer Deposited Ni/ZrO_2-SiO_2 for Combined Capture and Oxidation of VOCs. *ACS Appl. Mater. Interfaces* **2020**, *12* (35), 39318−39334.
(33) Guillemot, M.; Mijoin, J.; Mignard, S.; Magnoux, P. Volatile Organic Compounds (VOCs) Removal over Dual Functional Adsorbent/Catalyst System. *Appl. Catal., B* **2007**, *75* (3−4), 249−255.
(34) Xie, Z. Z.; Wang, L.; Cheng, G.; Shi, L.; Zhang, Y. B. Adsorption Properties of Regenerative Materials for Removal of Low Concentration of Toluene. *J. Air Waste Manage. Assoc.* **2016**, *66* (12), 1224−1236.
(35) Wang, Y.; Yang, D.; Li, S.; Chen, M.; Guo, L.; Zhou, J. Ru/Hierarchical HZSM-5 Zeolite as Ef Fi Cient Bi-Functional Adsorbent/Catalyst for Bulky Aromatic VOCs Elimination. *Microporous Mesoporous Mater.* **2018**, *258*, 17−25.
(36) Urbutis, A.; Kitrys, S. Dual Function Adsorbent-Catalyst CuO-CeO_2/NaX for Temperature Swing Oxidation of Benzene, Toluene and Xylene. *Cent. Eur. J. Chem.* **2014**, *12* (4), 492−501.
(37) Huang, S.; Zhang, C.; He, H. In Situ Adsorption-Catalysis System for the Removal of o-Xylene over an Activated Carbon Supported Pd Catalyst. *J. Environ. Sci.* **2009**, *21* (7), 985−990.
(38) Sonar, S.; Giraudon, J.-M.; Kaliya Perumal Veerapandian, S.; Bitar, R.; Leus, K.; Van Der Voort, P.; Lamonier, J.-F.; Morent, R.; De Geyter, N.; Lofberg, A. Abatement of Toluene Using a Sequential Adsorption-Catalytic Oxidation Process: Comparative Study of Potential Adsorbent/Catalytic Materials. *Catalysts* **2020**, *10*, 761.
(39) Wu, J.; Xia, Q.; Xiao, J.; Li, Z. Chromium-Based Metal-Organic Framework MIL-101 as a Highly Effective Catalyst in Plasma for Toluene Removal Related Content Tars Removal by Non-Thermal Plasma and Plasma Catalysis. *J. Phys. D: Appl. Phys.* **2017**, *50*, 475202.
(40) Lawrence, P. S.; Grünewald, M.; Dietrich, W.; Agar, D. W. Optimal Distribution of Catalyst and Adsorbent in an Adsorptive Reactor at the Reactor Level. *Ind. Eng. Chem. Res.* **2006**, *45* (14), 4911−4917.
(41) Brazlauskas, M.; Kitrys, S. Synthesis and Properties of CuO/Zeolite Sandwich Type Adsorbent-Catalysts. *Chin. J. Catal.* **2008**, *29* (1), 25−30.
(42) Campbell, L.; Sanders, M. Sequential Adsorptive Capture and Catalytic Oxidation of Volatile Organic Compounds in a Reactor Bed. U.S. Patent US6033638A, March 1998.
(43) Kamal, M. S.; Razzak, S. A.; Hossain, M. M. Catalytic Oxidation of Volatile Organic Compounds (VOCs) - A Review. *Atmos. Environ.* **2016**, *140*, 117−134.
(44) Okumura, K.; Kobayashi, T.; Tanaka, H.; Niwa, M. Toluene Combustion over Palladium Supported on Various Metal Oxide Supports. *Appl. Catal., B* **2003**, *44* (4), 325−331.
(45) Zhao, T.; Jeremias, F.; Boldog, I.; Nguyen, B.; Henninger, S. K.; Janiak, C. High-Yield, Fluoride-Free and Large-Scale Synthesis of MIL-101(Cr). *Dalton Trans.* **2015**, *44* (38), 16791−16801.
(46) D'Amico, A. D.; Wu, D.; Hodgin, H. J. *Vapor Purification for the Micromeritics 3FLEX*.
(47) Li, S.; Zhu, H.; Qin, Z.; Wang, G.; Zhang, Y.; Wu, Z.; Li, Z.; Chen, G.; Dong, W.; Wu, Z.; et al. Morphologic Effects of Nano CeO_2−TiO_2 on the Performance of Au/CeO_2−TiO_2 Catalysts in Low-Temperature CO Oxidation. *Appl. Catal., B* **2014**, *144*, 498−506.
(48) Zhao, S.; Mei, J.; Xu, H.; Liu, W.; Qu, Z.; Cui, Y.; Yan, N. Research of Mercury Removal from Sintering Flue Gas of Iron and Steel by the Open Metal Site of Mil-101(Cr). *J. Hazard. Mater.* **2018**, *351*, 301−307.
(49) Vu, T. A.; Le, G. H.; Dao, C. D.; Dang, L. Q.; Nguyen, K. T.; Dang, P. T.; Tran, H. T. K.; Duong, Q. T.; Nguyen, T. V.; Lee, G. D. Isomorphous Substitution of Cr by Fe in MIL-101 Framework and Its Application as a Novel Heterogeneous Photo-Fenton Catalyst for Reactive Dye Degradation. *RSC Adv.* **2014**, *4* (78), 41185−41194.
(50) Krishnamurthy, A.; Thakkar, H.; Rownaghi, A. A.; Rezaei, F. Adsorptive Removal of Formaldehyde from Air Using Mixed-Metal Oxides. *Ind. Eng. Chem. Res.* **2018**, *57* (38), 12916−12925.
(51) Neimark, A. V.; Thommes, M.; Sing, K. S. W.; Rodriguez-Reinoso, F.; Olivier, J. P.; Kaneko, K.; Rouquerol, J. Physisorption of Gases, with Special Reference to the Evaluation of Surface Area and Pore Size Distribution (IUPAC Technical Report). *Pure Appl. Chem.* **2015**, *87* (9−10), 1051−1069.
(52) Huang, C.-Y.; Song, M.; Gu, Z.-Y.; Wang, H.-F.; Yan, X.-P. Probing the Adsorption Characteristic of MetalÀOrganic Framework MIL-101 for Volatile Organic Compounds by Quartz Crystal Microbalance. *Environ. Sci. Technol.* **2011**, *45*, 4490−4496.
(53) Sing, K. S. W. Reporting Physisorption Data for Gas/Solid Systems with Special Reference to the Determination of Surface Area and Porosity (Provisional). *Pure Appl. Chem.* **1982**, *54* (11), 2201−2218.
(54) Baek, S.-W.; Kim, J.-R.; Ihm, S.-K. Design of Dual Functional Adsorbent/Catalyst System for the Control of VOC's by Using Metal-Loaded Hydrophobic Y-Zeolites. *Catal. Today* **2004**, *93*−*95*, 575−581.
(55) Huang, Q.; Malekian, A. Optimization of PSA Process for Producing Enriched Hydrogen from Plasma Reactor Gas. *Sep. Purif. Technol.* **2008**, *62* (1), 22−31.
(56) Ncube, T.; Kumar Reddy, K. S.; Al Shoaibi, A.; Srinivasakannan, C. Benzene, Toluene, m-Xylene Adsorption on Silica-Based Adsorbents. *Energy Fuels* **2017**, *31* (2), 1882−1888.
(57) Mokhatab, S.; Poe, W.; Mak, J. Y. *Handbook of Natural Gas Transmission and Processing - Gulf Professional Publishing* **2015**, 1−597.
(58) Kim, K. H.; Szulejko, J. E.; Raza, N.; Kumar, V.; Vikrant, K.; Tsang, D. C. W.; Bolan, N. S.; Ok, Y. S.; Khan, A. Identifying the Best Materials for the Removal of Airborne Toluene Based on Performance Metrics - A Critical Review. *J. Cleaner Prod.* **2019**, *241*, 118408.
(59) Haghighi, E.; Zeinali, S. Formaldehyde Detection Using Quartz Crystal Microbalance (QCM) Nanosensor Coated by Nanoporous MIL-101 (Cr) Film. 2020. *Microporous Mesoporous Mater.* **2020**, *300*, 110065.

https://doi.org/10.1021/acs.energyfuels.1c01950
Energy Fuels XXXX, XXX, XXX−XXX